Nanostructured equimolar ceria-praseodymia for NOx-assisted soot oxidation: Insight into Pr dominance over Pt nanoparticles and metal–support interaction

Tahrizi Andana[a,b], Marco Piumetti[a], Samir Bensaid[a,*], Laurent Veyre[b], Chloé Thieuleux[b],
Nunzio Russo[a], Debora Fino[a], Elsje Alessandra Quadrelli[b], Raffaele Pirone[a]

[a] Department of Applied Science and Technology, Politecnico di Torino, Corso Duca degli Abruzzi 24, 10129, Turin, Italy
[b] Université de Lyon 1, ICL, C2P2 UMR 5265, CPE Lyon, 43 Bd du 11 Novembre 1918, F-69616, Villeurbanne, France

ARTICLE INFO

ABSTRACT

This work compares the catalytic activity of nanostructured ceria-praseodymia impregnated with Pt nanoparticles stabilized by *n*-octylsilane (Pt/Ce50Pr50-NP), with pure ceria nanoparticles (Ce-NP), ceria-praseodymia (Ce50Pr50-NP) and Pt on ceria (Pt/Ce-NP). The idea behind these structures stems from the fact that both Pt/ceria and Ce-Pr mixed oxide are effective towards CO, NO and soot oxidations, as well as for the NOx-assisted soot oxidation. The oxide supports have been prepared via a hydrothermal synthesis. Catalytic activity tests have shown the effectiveness of Ce50Pr50-NP towards the NOx-assisted soot oxidation. The intrinsic activity of this material is even higher than the Pt/Ce-NP counterpart. This finding seems related to the adsorption of NO_2 onto ceria-praseodymia. The addition of Pt on the Ce50Pr50-NP surface appears unnecessary as the effect of Pr on the catalytic activity prevails. The samples have also been thermally aged and their catalytic performances have been compared. A smaller decrease in activity has been observed for Ce50Pr50-NP, compared to Ce-NP, and it has been linked to the material's persistent adsorptive properties. The deposited Pt nanoparticles on the surface of Ce50Pr50-NP, however, have suffered from sintering after the thermal aging, and therefore both aged Pt/Ce50Pr50-NP and Ce50Pr50-NP have comparable catalytic performances.

1. Introduction

Investigation into ceria-based catalysts has been part of long-standing efforts to minimize the exposure of Diesel soot (officially known as "particulate matter"/PM) to air. Pure ceria, normally designed as a porous material with high surface area, is naturally capable of helping lower soot abatement reaction temperature thanks to its unique redox or oxygen-storing properties [1–5]. Unfortunately, conventional, monometallic oxide ceria has been proved insufficient for meeting current needs in automotive catalysis as the emission standards have become more stringent due to the implementation of Euro 6. Consequently, more attention must be paid to improving the catalytic properties of ceria in order that the prospect of ceria-based catalysts for automotive applications be perpetually promising.

We have started the campaign by downsizing and shaping ceria particles to well-defined nanostructures. The famous nanocubic structure grants ceria low specific surface area and well-defined six (100) surfaces that are very reactive towards soot oxidation [6–8]. This

material even outperforms microstructured ceria that notably has much higher surface area. We have also developed an interest in embedding foreign metals into nanostructured ceria as a means of improving redox properties and reducibility. In the past, we have discerned the effect of zirconium and praseodymium on ceria; while the former renders ceria more thermally stable at high temperature, the latter endorses high reducibility and high surface oxygen species [9–11]. In our recent work, we have maximized the performance of platinum and copper catalysts supported by nanostructured ceria in NOx-assisted soot oxidation. We have successfully prepared small metal nanocatalysts (2–4 nm in diameter) via an organometallic route, that is the stabilization of Pt and Cu nanoparticles by an organosilane compound [12,13].

In the present work, we bring back our investigation into ceria-praseodymia catalysts with the major focus on nanostructured equimolar ceria-praseodymia (denoted herewith as Ce50Pr50). In the past, we limited our scope of work to the effect of the catalysts on normal soot oxidation. In this work, we have expanded the application to NO oxidation and NOx-assisted soot oxidation. The early insight into

Ce50Pr50 catalytic activity towards NO_x-related oxidation has been provided by Krishna et al., who concluded that at equimolar composition cerium and praseodymium mixed oxide was very active towards NO oxidation, hence high NO_x-assisted soot oxidation activity [14]. Guillén-Hurtado et al. have demonstrated that high surface equimolar ceria-praseodymia catalyst ($125\,m^2\,g^{-1}$) synthesized via microemulsion also resulted in high catalytic activity, even outperforming the conventional 1%-wt Pt/Al_2O_3 catalyst [15]. Our current investigation featured nanostructured equimolar ceria-praseodymia sample (Ce50Pr50-NP) that has been prepared via hydrothermal synthesis and has a much lower surface area ($16\,m^2\,g^{-1}$) [9]. To the best of our knowledge, this type of material has never been reportedly tested with NO oxidation and NO_x-assisted soot oxidation.

We have tested in parallel pure nanocubic ceria (denoted herewith as Ce-NP) and ceria catalysts (pure and in an equimolar mixture with praseodymia) impregnated with small, silane-stabilized Pt nanoparticles (denoted herein as Pt/Ce-NP and Pt/Ce50Pr50-NP, respectively). Of particular interest is the last catalyst in the series (Pt/Ce50Pr50-NP), which is the combination of two powerful materials for NO oxidation and NO_x-assisted soot oxidation. In this case, we would like to observe the dominance of Pt and Ce50Pr50 during the reaction.

2. Experimental

2.1. Catalyst synthesis

The synthesis began with dissolving equimolarly $Ce(NO_3)_3 \cdot 6H_2O$ and $Pr(NO_3)_3 \cdot 6H_2O$ (5 mmol, each, Sigma-Aldrich) in 10 ml deionized water. NaOH pellets (1.2 mmol, Sigma-Aldrich) were dissolved in 70 ml deionized water and stirred. The solution of salt precursors was then added dropwise into the continuously stirring NaOH solution, followed by the formation of pale green slurry. The mixture was left for an additional stirring for 1 h. The final slurry was transferred to an autoclave (200 ml) in which deionized water was added to reach minimum 75% of the total autoclave volume. The autoclave was then thermally treated in a furnace at 180 °C for 24 h. The fresh precipitates were then separated from their supernatant by centrifugation, washed with ethanol and deionized water several times, and dried at 60 °C overnight. Finally, the dry solids were gently ground and calcined at 550 °C for 4 h. The pure, nanocubic ceria sample (Ce-NP) as the reference material has also been prepared by using the exact same procedure with that of Ce50Pr50-NP; the difference was only in the salt precursor (10 mmol of $Ce(NO_3)_3 \cdot 6H_2O$ was used, instead).

$Pt(dba)_2$ was used as the precursor for Pt nanoparticles and prepared according to the literature [16]. The silane-stabilized Pt nanoparticles have been prepared according to Pelzer et al. [17]. The Pt nanoparticles were obtained as a dark brown colloid (0.05 mmol) by mixing $Pt(dba)_2$ (0.05 mmol) and $Si(n\text{-}C_8H_{17})$ (Sigma-Aldrich) (0.05 mmol) in dry THF (34 ml) in a Schlenk flask under Ar which was then transferred to a high-pressure glass reactor for a reaction under 3 bar of H_2.

1%-wt loading of Pt nanoparticles, with respect to the weight of the ceria support, was achieved by wetness impregnation (WI). Pure ceria (Ce-NP) and ceria-praseodymia (Ce50Pr50-NP) were used as the support. The final colloid of Pt nanoparticles was concentrated via vacuum evaporation till the adequate volume was reached. The concentrated colloid was carefully impregnated dropwise onto the support under flowing Ar. The wet support was left overnight under air at ambient temperature to allow drying. Finally, the Pt-impregnated catalysts, denoted as Pt/Ce-NP and Pt/Ce50Pr50-NP, were air-dried at 120 °C for 2 h to remove the remaining solvent and then air-calcined at 320 °C for 10 h to remove the ungrafted ligands.

2.2. Catalyst characterization

Powder X-ray diffractograms were collected by an X'Pert Philips PW3040 diffractometer using Cu Kα radiation. The measurement parameters used in the analysis are as follows: 2θ range between 20 and 70°, step size of 0.013° and counting time at 0.2 s/step. The assignment of peaks referred to the Powder Diffraction Files by International Centre of Diffraction Data (ICDD). The crystallite size was calculated by using Scherrer's equation, in which the peak broadening was corrected with respect to that of an instrument calibration standard (LaB_6).

N_2 physisorption analysis was carried out in a Tristar II 3020 Micromeritics instrument to determine BET surface area and pore volume of the prepared catalysts. Before the analysis, the catalyst was pre-heated at 200 °C for 2 h under vacuum. The specific surface area was finally calculated via BET (Brunauer-Emmett-Teller) method, and thus denoted as S_{BET}.

Platinum content in the samples was analyzed via an inductively coupled plasma atomic emission spectroscopy (ICP-AES) at Politecnico di Torino, Italy

Sample morphology was observed via a field emission scanning electron microscopy, using a FESEM Zeiss MERLIN, Gemini-II (Politecnico di Torino, Italy) and a high-resolution transmission electron microscopy (HRTEM, JEOL 2100FEG microscope at the "Centre Technologique des Microstructures", CTμ, Villeurbanne, France).

X-ray photoelectron spectroscopy was performed in a PHI Versa probe apparatus using a band-pass energy of 187.85 eV, a 45° take off angle and a 100.0 μm diameter X-ray spot size. O, Ce and Pt oxidation states on the surface were eventually interpreted from the deconvoluted spectra.

Sample reducibility was analyzed via CO-TPR (temperature-programmed reduction). The analysis was carried out in a fixed-bed Quartz U-tube micro reactor (ID = 4 mm) containing 150 mg of silica and 45 mg of catalysts. During the analysis, the reactor was heated by a PID-controlled furnace (from ambient temperature to 800 °C with a heating rate at $10\,°C\,min^{-1}$) and then put in contact with reducing flowing gas (2000 ppm CO in N_2, $300\,ml\,min^{-1}$). CO consumption and CO_2 production were continuously recorded in NDIR analyzers (ABB Uras 14). Before analysis, sample was pretreated with synthetic air for 2 h followed by flushing with N_2 for 30 min.

2.3. Catalytic activity test

To carry out catalytic activity tests, a general setup for TPO (Temperature-Programmed Oxidation) was prepared. The apparatus was comprised of a PID-regulated furnace, a quartz U-tube reactor with a fixed catalytic bed, a K-type thermocouple, a continuous NDIR gas analyzer (ABB Uras 14) for CO and CO_2 detection and an Emerson XStream X2GP gas analyzer for NO, NO_2 and O_2 detection. The reactor setup enabled a bypass line, through which gases containing pollutants (i.e. CO and NO) initially flowed to allow gas concentration stabilization. In the present work, we have carried out four catalytic activity tests that varied in catalytic bed and test's sequence

2.4. CO oxidation

In this test, the catalytic bed contained 100 mg of catalyst. Before the test, the catalyst was pre-heated at 100 °C for 30 min under $50\,ml\,min^{-1}$ of air. The reactor was then cooled at a rate of $5\,°C\,min^{-1}$ to 50 °C. During the cooling process, a mixture of 1000 ppm-v CO and 10%-v O_2 in N_2 was sent at a rate of $50\,ml\,min^{-1}$ to the bypass line. After the stabilization of CO and O_2 concentrations, the flow was sent back to the reactor and gradual heating started at a rate of $5\,°C\,min^{-1}$. The test proceeded until the reactor temperature reached 500 °C.

2.5. NO oxidation

In this test, the catalytic bed contained a mixture of 150 mg of SiO_2 (Umicore) and 45 mg of catalyst (gently stirred with spatula for 3 min). Before the test, the catalyst was normally pre-heated at 100 °C for

30 min under $100\,ml\,min^{-1}$ of 20%-v O_2 in N_2. The reactor was then cooled at a rate of $5\,°C\,min^{-1}$ to 50 °C. During the cooling process, a mixture of 550 ppm-v NO and 10%-v O_2 in N_2 was sent at a rate of $100\,ml\,min^{-1}$ to the bypass line. After the stabilization of NO, NO_2 and O_2 concentrations, the flow was sent back to reactor and the programmed heating started. The test was carried out in two modes: ramp and isothermal. In the first mode, the reactor heating was continuous and adjusted at a rate of $5\,°C\,min^{-1}$. In the second mode, the reactor was heated stepwise by 50 °C; the temperature of each step was kept constant for an isothermal treatment till the stabilization of NO, NO_2 and O_2 concentrations. In both cases, the heating was programmed to rise from 50 to 650 °C.

2.6. Soot oxidations

There were two catalytic tests with soot oxidation: (1) NO_x-free soot oxidation, in which only oxygen was used as the oxidant, and (2) NO_x-assisted soot oxidation, in which NO was also present in the feed. In the former test, the catalytic bed contained a loose mixture of 150 mg of SiO_2 (Umicore), 5 mg of soot (Printex-U, Degussa) and 45 mg of catalyst (gently stirred with spatula for 3 min). Before the test, the catalyst was pre-heated at 100 °C for 30 min under $100\,ml\,min^{-1}$ of N_2. The stream containing 10%-v O_2 in N_2 was sent at a rate of $100\,ml\,min^{-1}$ directly to the reactor. The gradual heating of the reactor started afterwards at a rate of $5\,°C\,min^{-1}$ from ambient temperature to 700 °C. In the latter test, the catalytic bed comprised a loose mixture of 150 mg of SiO_2 (Umicore), 5 mg of model soot (Printex-U, Degussa) and 45 mg of catalyst (gently stirred with spatula for 3 min). Before the test, the catalyst was pre-heated at 100 °C for 30 min under $100\,ml\,min^{-1}$ of 20%-v O_2 in N_2. The reactor was then cooled at a rate of $5\,°C\,min^{-1}$ to 50 °C. During the cooling process, a mixture of 550 ppm-v NO and 10%-v O_2 in N_2 was sent at a rate of $100\,ml\,min^{-1}$ to the bypass line. After the gas saturation, the flow was sent back to the reactor and the gradual heating started at a rate of $5\,°C\,min^{-1}$. The test proceeded until the reactor temperature reached 700 °C.

The series of soot oxidation tests was finally concluded by isothermal catalytic tests, in which soot was oxidized isothermally at 400 °C. The test used the same reactor bed and gas feed conditions with the ones of the test with NO_x-assisted soot oxidation. A mixture of 550 ppm-v NO and 10%-v O_2 in N_2 was initially sent at a rate of $100\,ml\,min^{-1}$ to the bypass line. The reactor was then heated gradually to 400 °C at a rate of $10\,°C\,min^{-1}$. After the gas saturation, the flow was sent back to the reactor. The temperature was kept constant at 400 °C until the concentration of CO_2 was close to zero.

2.7. Catalyst stability

In order to analyze the thermal and catalytic stability of the prepared catalysts, the catalytic activity of "fresh" and "aged samples" has been considered. The "aged samples" were obtained by a thermal aging at 700 °C for 8 h before the catalytic tests. Both the reactor bed condition and the experimental procedure used for the assessment of the catalytic performances of aged samples, were the same as those used for the NO_x-assisted soot oxidation over fresh-samples.

3. Result and discussion

3.1. Catalyst textural properties

Table 1 summarizes the BET surface areas and pore volumes of the sample. Ce-NP has a very low surface area $(8\,m^2\,g^{-1})$ due to the low amount of interparticle voids. On the other hand, Ce50Pr50-NP has higher surface area $(16\,m^2\,g^{-1})$ than Ce-NP, thus suggesting a significant morphological change in the sample. The surface areas of Pt-impregnated catalysts appear similar to those of the pure supports. The aged samples generally demonstrate lower BET surface areas $(4\,m^2\,g^{-1}$

and $10\,m^2\,g^{-1}$ for Ce-NP and Ce50Pr50-NP, respectively) and this naturally occurs due to sintering. ICP-AES analysis has estimated that Pt/Ce-NP and Pt/Ce50Pr50-NP contain about 0.87%-wt and 0.64%-wt of Pt, respectively.

Due to the low quantity of platinum in the impregnated samples (less than 1%-wt), we performed XRD analysis only on the bare supports (Ce-NP and Ce50Pr50-NP). Fig. 1 shows the X-ray diffractograms of the fresh (Fig. 1A) and aged supports (Fig. 1B). We also include the diffractogram of fresh praseodymium oxide or praseodymia (PrO_x), labelled herein as "Pr-NP", prepared through the same hydrothermal synthesis (*vide supra*) using only $Pr(NO_3)_3 \cdot 6H_2O$ as the precursor. On Fig. 1A, the diffractograms of Ce-NP, Ce50Pr50-NP and Pr-NP seem very similar to each other; their peaks can simply be attributed to a classical fluorite-like cubic structure according to the literature [9,15]. Despite the similarity in crystal structure, there is a slight difference in the peak position among the diffractograms and it varies with praseodymia content in the sample. A very small peak shift to higher 2θ with respect to the peak position of Ce-NP is observed for Ce50Pr50-NP. The 2θ difference, as indicated by the green-orange labels on Fig. 1A, ranges from $+0.04°$ to $+0.08°$. With respect to the peak position of Pr-NP, a much higher peak shift to higher 2θ is observed. The 2θ difference spans from $+0.40°$ to $+0.84°$ and it gradually increases with 2θ. This suggests that even at the equimolar composition, a solid solution between ceria and praseodymia still structurally behaves as ceria as if praseodymia were well-dispersed in the ceria matrix. Table 1 presents the crystallite sizes of the supports calculated using Scherrer's equation. The crystallite size of fresh Ce50Pr50-NP seems smaller than that of fresh Ce-NP and this trend may reflect the particle size trend of the samples (observable through sample micrography). Table 1 also displays the intensity ratio of (220) and (222) peaks to (200) peak. The ratios are somewhat similar for both Ce-NP and Ce50Pr50-NP, although they are slightly higher for Ce-NP.

The aged supports give much more interesting information than their fresh counterparts. Fig. 1B shows the diffractograms of aged Ce-NP (orange curve) and Ce50Pr50-NP (green curve, topmost) samples. A very small peak shift to higher 2θ with respect to the peak position of aged Ce-NP is observed for aged Ce50Pr50-NP. The 2θ difference spans from $+0.01°$ to $+0.07°$. The peak shifts observed for the aged samples seem lower than those observed for the fresh samples (Fig. 1A). In addition, the peak positions of aged Ce-NP are somewhat similar to those of fresh Ce-NP. This means that for aged Ce50Pr50-NP a shift to lower 2θ with respect to the peak position of fresh Ce50Pr50-NP is observed and this phenomenon resembles the behavior of Pr-NP. This finding gives the initial insight into possibility of segregation of praseodymia from ceria matrix after thermal aging. The crystallite sizes of the aged samples, as reported on Table 1, vary among the samples. While the decrease in crystallite size is observed for aged Ce-NP, the increase in size is instead observed for Ce50Pr50-NP. The peak intensity ratios [(220)/(200) and (222)/(200)] of the two supports are significantly higher after the thermal aging. The increase is even higher in the case of Ce-NP, especially in (222)/(200) ratio. This foresees how the morphology of the sample alters after the thermal aging, possibly due to a post-aging surface truncation (the rise of high-index planes on the surface) as suggested elsewhere [7].

Fig. 2A–B shows the FE-SEM images of Ce-NP and Ce50Pr50-NP supports. As widely discussed in the literature [6,7,18,19], the hydrothermal synthesis is shape-oriented, hence it always results in well-defined nanostructures. The morphology of Ce-NP, as seen on Fig. 2A, is nanocube, comprised of six smooth (100) facets. The size of large nanocubes varies from 100 to 300 nm, while smaller nanocubes can exist from 30 to 50 nm. Equimolar mixing with praseodymia evidently favors growth orientation towards nanorods. As seen on Fig. 2B, nanocubes also exist in Ce50Pr50-NP, however their average dimension is substantially smaller than that in Ce-NP. Fig. 2C–D shows the TEM images of the supports. The size of the nanocubic Ce-NP (Fig. 2C) is around 100 nm and the darker shades observed in the image reflects the

Table 1
Textural properties and platinum content of the prepared samples.

Sample	N$_2$ physisorption		X-ray diffraction			Pt content (%-wt.)[c]
	S_{BET} (m^2 g^{-1})[a]	$V_{p,t}$ (cm^3 g^{-1})[a]	Crystallite size (nm)[b]	(220)/(200) intensity ratio	(222)/(200) intensity ratio	
Ce-NP	8 (fresh)	0.02 (fresh)	69 (fresh)	1.62 (fresh)	0.24 (fresh)	–
	4 (aged)	0.01 (aged)	43 (aged)	3.17 (aged)	0.66 (aged)	
Ce50Pr50-NP	16 (fresh)	0.04 (fresh)	24 (fresh)	1.55 (fresh)	0.21 (fresh)	–
	10 (aged)	0.02 (aged)	43 (aged)	2.04 (aged)	0.29 (aged)	
Pt/Ce-NP	8	0.02	–			0.87
Pt/Ce50Pr50-NP	16	0.04	–			0.64

[a] obtained from N$_2$ physisorption at −196 °C.
[b] calculated using Scherrer's equation.
[c] analyzed via an ICP-AES.
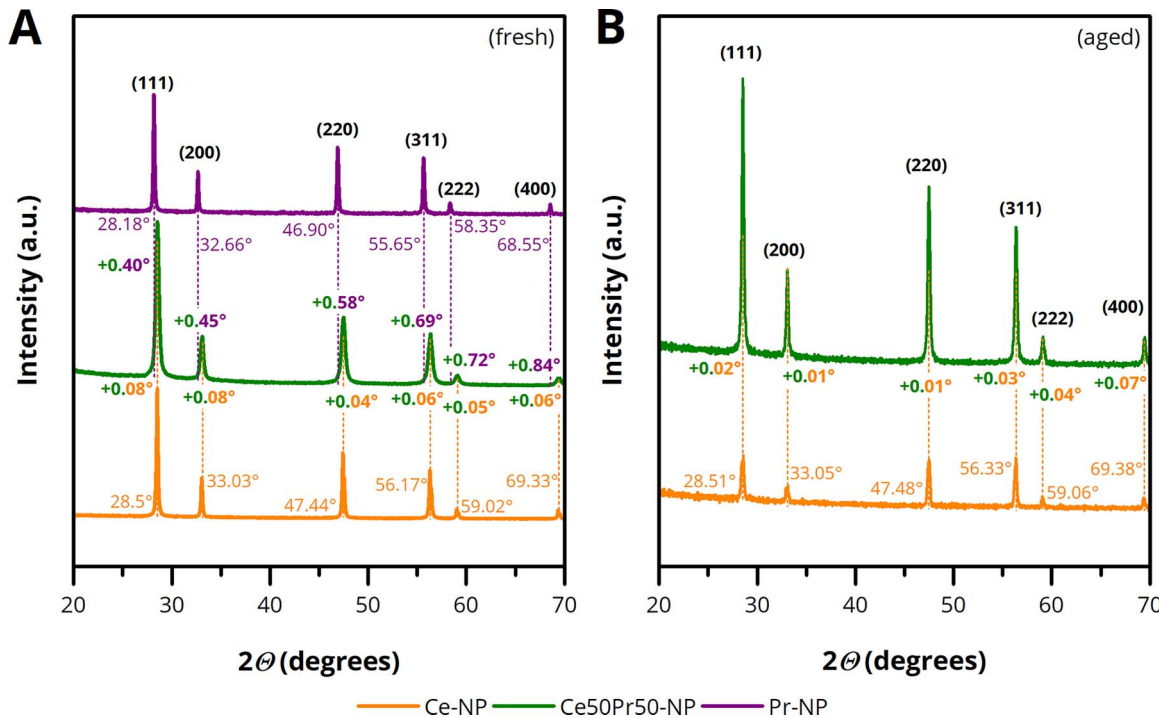
Fig. 1. X-ray diffractograms of (A) fresh and (B) aged unimpregnated catalysts.

significant thickness of the particle. Meanwhile, some approximately 100 nm-long nanorods are observed in the micrograph of Ce50Pr50-NP (Fig. 2D) and their diameters are about 20 nm average.

Fig. 3 shows various TEM images of the platinum-containing samples. In addition, STEM-HAADF images and their corresponding STEM-EDX spectra are summarized on Fig. 4 to better observe the distribution of Pt and the effect of thermal aging. The images in the first row of Fig. 3 [Fig. 3(i)] are the micrographs of the fresh Pt/Ce-NP sample. In line with our previous work [20], stabilization by *n*-octylsilane results in Pt nanoparticles whose dimension ranges narrowly from 2 to 4 nm. Two strong lattice fringes on the last figure in the row [Fig. 3C(i)], according to the FFT image analysis, can be ascribed to CeO$_2$(111) and Pt(111) with the measured interplanar distances (*d*-spacing) of 0.315 nm and 0.22 nm, respectively. Table S1 (Supporting Information) presents more details concerning the results of the FFT image analysis. On Fig. 4(i), a good deposition of the nanoparticles onto Ce-NP support is observed on the STEM-HAADF image (Pt nanoparticles are seen as "bright spots"), as they appear evenly distributed on the surface. The images of the third row of Fig. 3 [Fig. 3(iii)] belong to fresh Pt/Ce50Pr50-NP. The nanorods structure remain intact, yet the deposition of Pt seems less even on the surface of ceria-praseodymia. It is further confirmed by the STEM-HAADF image [Fig. 4(iii)]. The attachment of

Pt nanoparticles to Ce50Pr50-NP surface seems to be more difficult than that to Ce-NP and appears only on the nanorods. On Fig. 4C(iii), a small particle appears deposited on a big surface exhibits lattice fringes with *d*-spacing of about 0.196 nm can be ascribed to Pt(200).

The images in the second row [Fig. 3(ii)] are the micrographs of aged Pt/Ce-NP. On the first image in the row [Fig. 3A(ii)], small spherical particles with darker shades (possibly Pt due to higher molecular weight) appear around a nanocube, while in the next image [Fig. 3B(ii)], a larger particle (about 20 nm), possibly a Pt nanoparticle, appears deposited on a big surface of presumably ceria. FFT image analysis of two strong lattice fringes coming from two different zones on Fig. 3C(ii) characterizes the presence of Pt(200) and CeO$_2$(200) with *d*-spacing of 0.19 nm and 0.275 nm, respectively. Here, the size of possibly a sintered Pt nanoparticle is even higher (almost 30 nm). From the STEM-HAADF image [Fig. 4(ii)], it can also be observed that the sintered Pt nanoparticles are also present in a smaller dimension (about 10 nm), yet the size distribution of the particles becomes wider. Finally, the images in the last row [Fig. 3(iv)] belong to aged Pt/Ce50Pr50-NP. The first figure in the row [Fig. 3A(iv)] shows a slight enlargement of the nanorod. The results of the FFT image analysis on a random nanorod are subsequently displayed on Fig. 3B(iv). Two strong fringes that appear intersecting with each other with *d*-spacing of 0.31 nm and
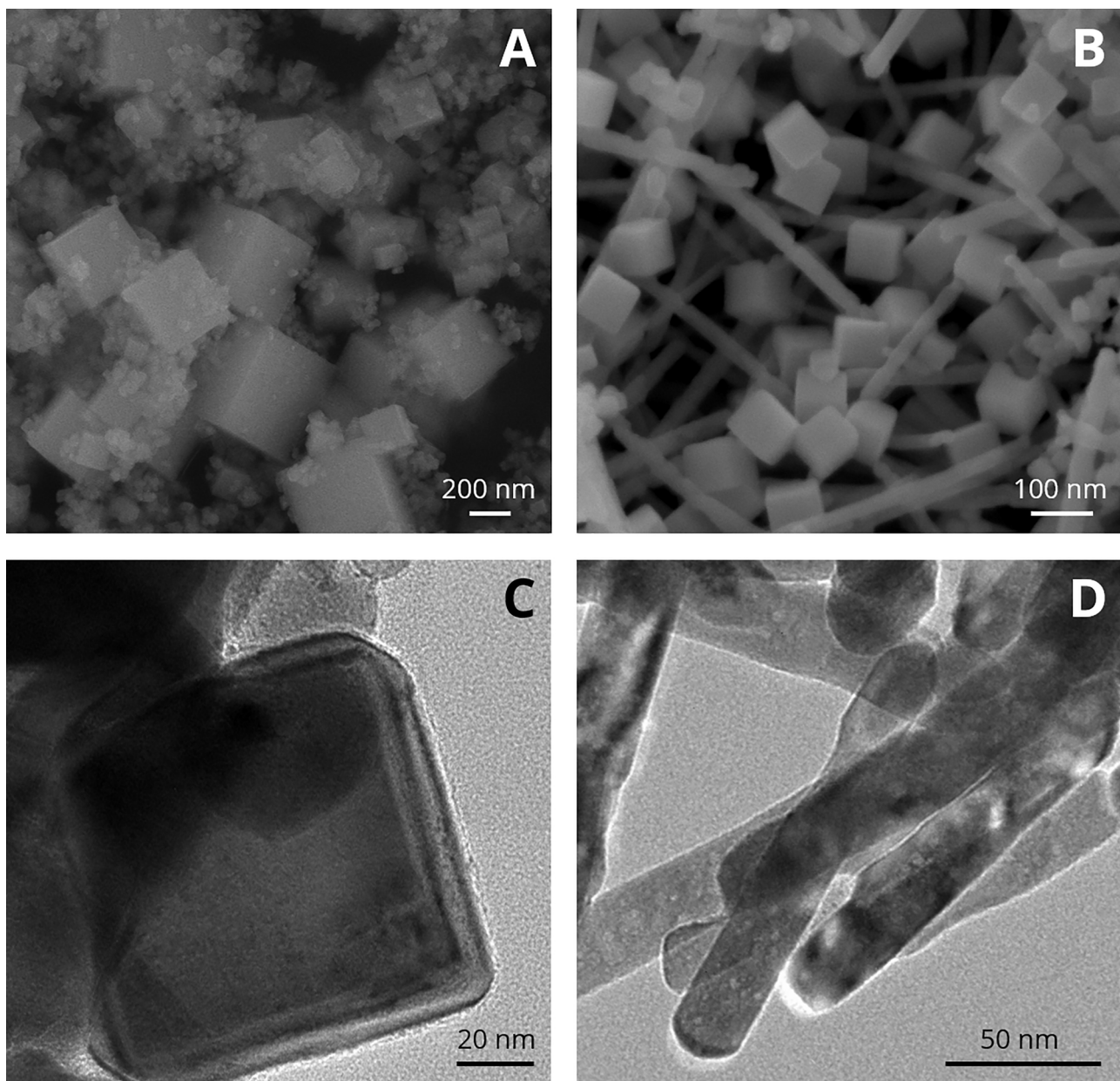
Fig. 2. FE-SEM and TEM images of Ce-NP (A and C) and Ce50Pr50-NP (B and D).

0.19 nm may be ascribed to CeO$_2$(111) and CeO$_2$(220), respectively. The appearance of fringes with *d*-spacing of 0.32 nm may instead be ascribed to PrO$_x$(111). However, one must pay attention that ceria and praseodymia share a great similarity in crystal structure, therefore this finding cannot be indicative of phase segregation of the two oxides. The STEM-HAADF image [Fig. 4(iv)] shows the appearance of spherical agglomerates, which may characterize either the phase change of ceria-praseodymia or the sintered Pt nanoparticle.

Fig. 4 also includes the STEM-EDX spectra of the selected points on the corresponding STEM-HAADF images of all Pt-containing samples. Spectrum 1 and 2 characterize Point 1 on the image of fresh Pt/Ce-NP and Point 2 on the image of aged Pt/Ce-NP. The presence of Ce and O signals in both spectra may simply refer to the cerium oxide support, as the intensity of the two elements in both spectra seems comparable. However, the intensity of Pt element appears lower in Spectrum 2. This suggests the lower abundance of Pt in the aged sample. Spectrum 3 and 4 characterize Point 3 and 4 on the image of fresh Pt/Ce50Pr50-NP, which are presumably Pt nanoparticles. The presence of Ce, O and additionally Pr seems inevitable in the two spectra and the similar

intensity of these elements can simply lead to the presence of Ce50Pr50-NP support. The intensity of Pt in Point 4 appears slightly higher than in Point 3, nevertheless the abundances of Pt in both spectra remain comparable. Spectrum 5 and 6 finally characterize Point 5 and 6 on the image of aged Pt/Ce50Pr50-NP. It can be quickly noticed that the two spectra lack in similarity. While in Spectrum 5 the presence of Ce50Pr50-NP is still confirmed albeit in a lower abundance, in Spectrum 6 only Pt element is observed. As seen on the corresponding micrograph on Fig. 3C(iv), Point 6 is actually an agglomerate whose presence is hardly observed in fresh Ce50Pr50-NP. This may be ascribed as a segregated Pt nanoparticle as a result of thermal aging.

3.2. Catalyst surface redox properties

The wide-scan XP spectra of the fresh samples are shown on Fig. S1–S4 (Supporting Information), while the surface composition (in atomic percentage) of the fresh samples is summarized on Table S2 (Supporting Information). The oxygen atomic percentage on the surface of ceria-praseodymia-supported catalysts is relatively lower than that
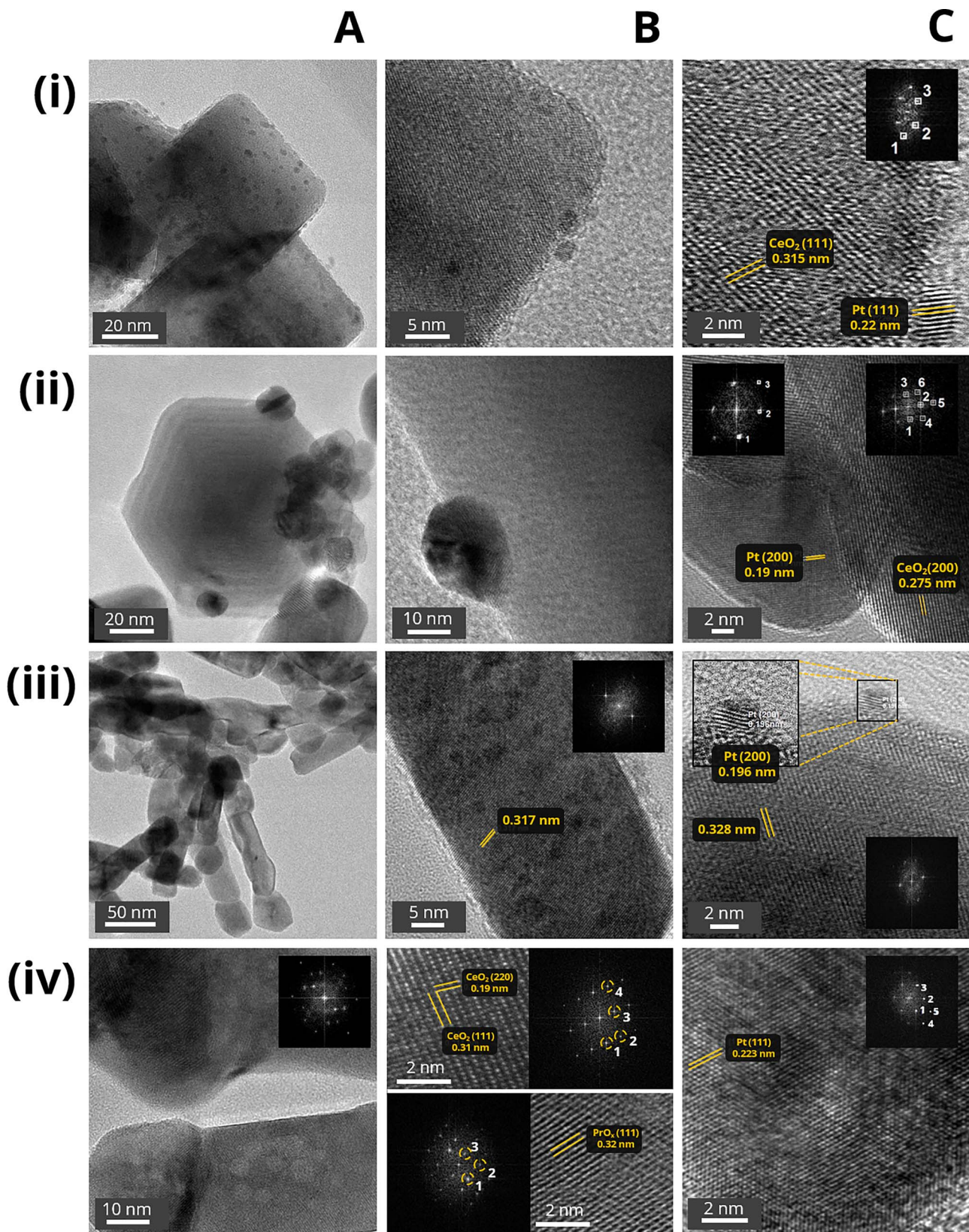
Fig. 3. Various TEM images of (i) fresh Pt/Ce-NP, (ii) aged Pt/Ce-NP, (iii) fresh Pt/Ce50Pr50-NP and (iv) aged Pt/Ce50Pr50-NP.

on the surface of ceria-supported ones. This may suggest the ability of praseodymium to reduce ceria and to generate defect sites (e.g. oxygen vacancies) on the surface. It can also be observed that the carbon percentage on the surface of ceria-praseodymia-supported catalysts is

higher than that on the surface of ceria-supported catalysts. The increase in defect sites presumably generated on the surface upon introducing praseodymium further gives rise to the increase in Ce^{3+}. The Lewis-basicity of this cerium species attracts CO_2, which is a Lewis acid,

● **oxygen** ● **cerium** ● **praseodymium** ● **platinum**
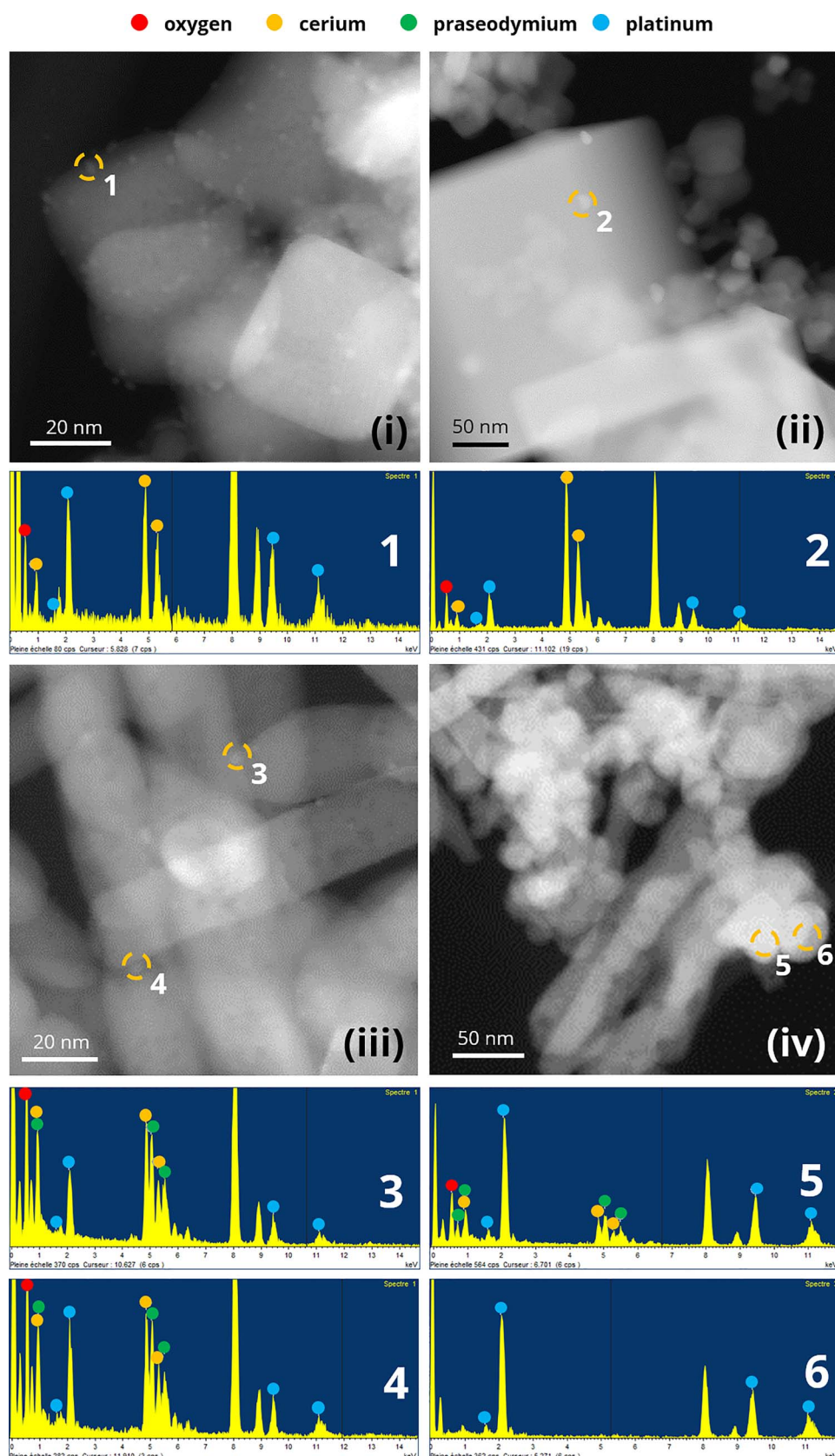
Fig. 4. STEM-HAADF images and STEM-EDX spectra of (i) fresh Pt/Ce-NP, (ii) aged Pt/Ce-NP, (iii) fresh Pt/Ce50Pr50-NP and (iv) aged Pt/Ce50Pr50-NP.

to adsorb to the site as carbonates species possibly during the calcination step, hence the increase in surface carbon content. Table S2 also reports the Pr-to-Ce ratio on the surface of the ceria-praseodymia samples. The ratio appears to be less than unity and therefore it

indicates that the defected cerium sites are more abundant than their praseodymium counterpart.

The wide-scan XP spectra of the aged samples are shown on Fig. S5–S8 (Supporting Information) and the corresponding surface
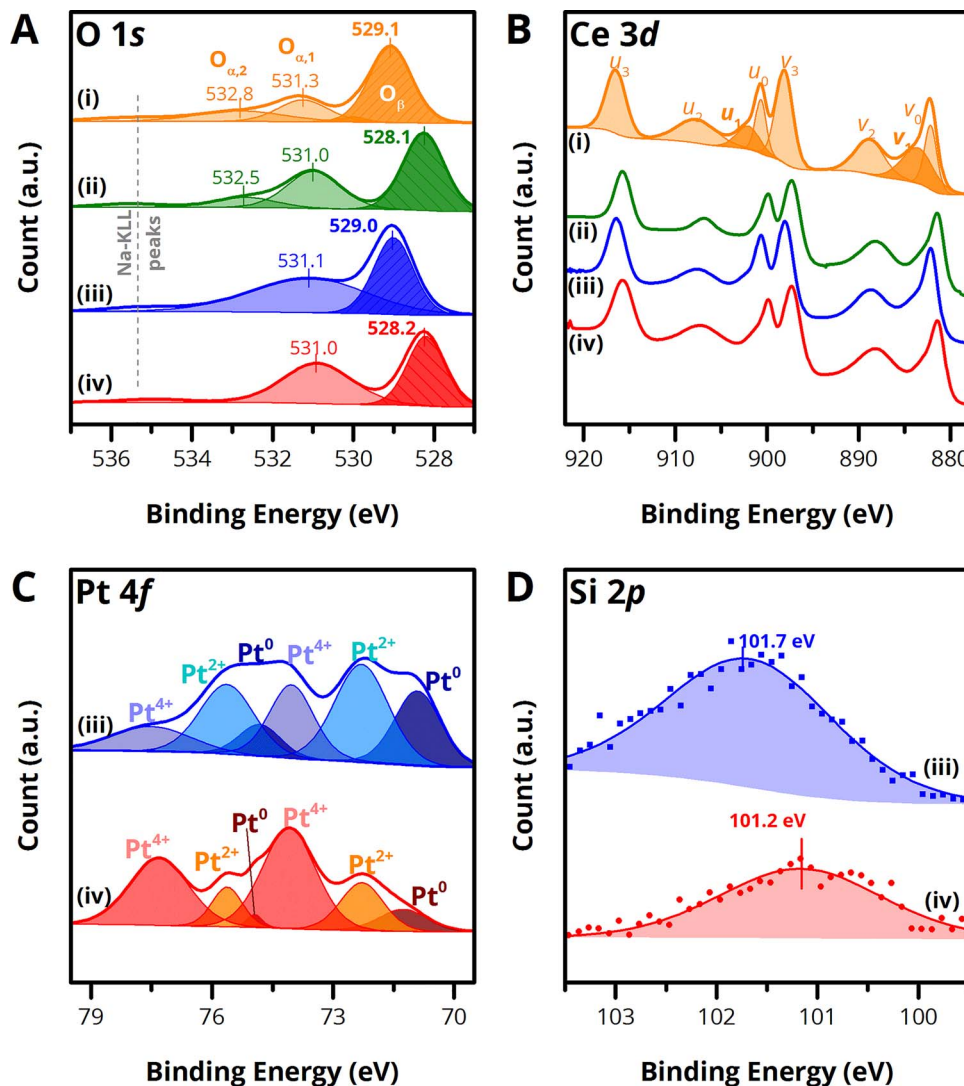
composition is also summarized on Table S2 (Supporting Information). The marked increase (about four times higher) in Ce concentration on the surface is observed for aged Ce-NP and Pt/Ce-NP samples while the concentration is rather constant on the surface of aged Ce50Pr50-NP and Pt/Ce50Pr50-NP. However, the Pr-to-Ce ratio on the surface of Pr-containing samples evidently increases after the thermal aging and the value is more than unity. This may indicate the segregation of praseodymia to the surface, as predicted earlier by the XRD analysis. The surface carbon content slightly decreases in the sample after the thermal aging, presumably due to the more oxidation/decomposition of carbonaceous impurities of the samples. The exposure of Pt post-aging becomes lower on the surface as it is evidenced by a decrease in surface Pt content (see Table S2). It is also interesting to observe the increase in silicon content on the surface of Pt-containing catalysts, especially on the surface of Pt/Ce50Pr50-NP. This may indicate the declining protective ability of the silicon to resist sintering, which will be further discussed in the next part.

Fig. 5A shows the deconvoluted O 1s spectra of the fresh samples that are generally constituted of: (1) peak of strong O−Ce bond in the binding energy (BE) range from 528.0 to 529.1 eV (denoted herein as O_β) [6,9,21], and surface oxygen species (denoted herein as O_α) in the BE range from 531.0 to 532.8 eV. In the spectra, Na-KLL Auger peaks also appear weakly between 535 and 536 eV and these peaks mark the residual sodium on the samples. Table 2 reports the relative abundances of these oxygen species for each sample.

It can be observed that the O_β peaks of the fresh Ce-NP and Pt/Ce-NP samples appear at slightly higher BE than those of the Ce50Pr50-NP and Pt/Ce50Pr50-NP samples. This may suggest the effect of mixing ceria and praseodymia at equimolar composition. The observed O_β peak position for ceria-praseodymia catalysts (528.1–528.2 eV) is somewhat similar to the one reported elsewhere and ascribed to the contribution from O − Pr bond [22]. From Fig. 5A, two peaks of O_α can be observed for the Pt-free catalysts: $O_{\alpha,1}$ that appears at BE range from 531.0 to 531.3 eV and $O_{\alpha,2}$ that appears at higher BE (532.5–532.8 eV). In general, the two species could be ascribed to any surface-capping/weakly-adsorbed oxygen species, such as OH^-, CO_3^{2-} and O^- species [23,24]. However, the relative abundance of $O_{\alpha,1}$ of Ce50Pr50-NP, as reported in Table 2, seems higher than that of Ce-NP, while the percentage of O_β seems lower. This might suggest that the presence of praseodymia in the sample weakens the O − Ce^{4+} bond on the surface and consequently gives rise to more O−Ce^{3+} species. Therefore, the $O_{\alpha,1}$ can be used to locate the potential surface defective sites, on which hydroxyl ions (OH^-) are normally found. Interestingly, the presence of $O_{\alpha,2}$ is observed only in the spectra of Pt-free catalysts. The species are hardly observed in the spectra of Pt-impregnated catalysts. This suggests that the $O_{\alpha,2}$ species benefits the surface attachment process during the impregnation. The species may be present in a form of carbonates (CO_3^{2-}) or carboxyl ($COOH^-$) since the use of high degree of basicity during the synthesis enables CO_2 adsorption.

Fig. 6A shows the O 1s spectra of the aged samples, deconvoluted in

Table 2
Relative abundances of O-species, Ce^{3+} ions and Pt species (%-atomic).

Sample	O_β	$O_{\alpha,1}$	$O_{\alpha,2}$
Ce-NP (fresh)	62	28	10
Ce-NP (aged)	69	31	–
Ce50Pr50-NP (fresh)	55	34	11
Ce50Pr50-NP (aged)	58	42	–
Pt/Ce-NP (fresh)	43	57	–
Pt/Ce-NP (aged)	52	48	–
Pt/Ce50Pr50-NP (fresh)	51	49	–
Pt/Ce50Pr50-NP (aged)	36	39	25

Sample	Ce^{3+}	Pt^0	Pt^{2+}	Pt^{4+}
Ce-NP (fresh)	21	–	–	–
Ce-NP (aged)	26	–	–	–
Ce50Pr50-NP (fresh)	24	–	–	–
Ce50Pr50-NP (aged)	17	–	–	–
Pt/Ce-NP (fresh)	21	25	47	28
Pt/Ce-NP (aged)	27	29	41	30
Pt/Ce50Pr50-NP (fresh)	23	8	24	68
Pt/Ce50Pr50-NP (aged)	18	25	24	51

the same fashion as those of the fresh samples (Fig. 5A). The bare supports, Ce-NP and Ce50Pr50-NP, now seem to only have two types of surface oxygens: one lattice-like oxygen species, O_β and one surface-capping oxygen species, $O_{\alpha,1}$ most likely present in a form of hydroxyls. This suggests that the thermal aging may induce decomposition of the weaker oxygen species ($O_{\alpha,2}$), which may further be related to the
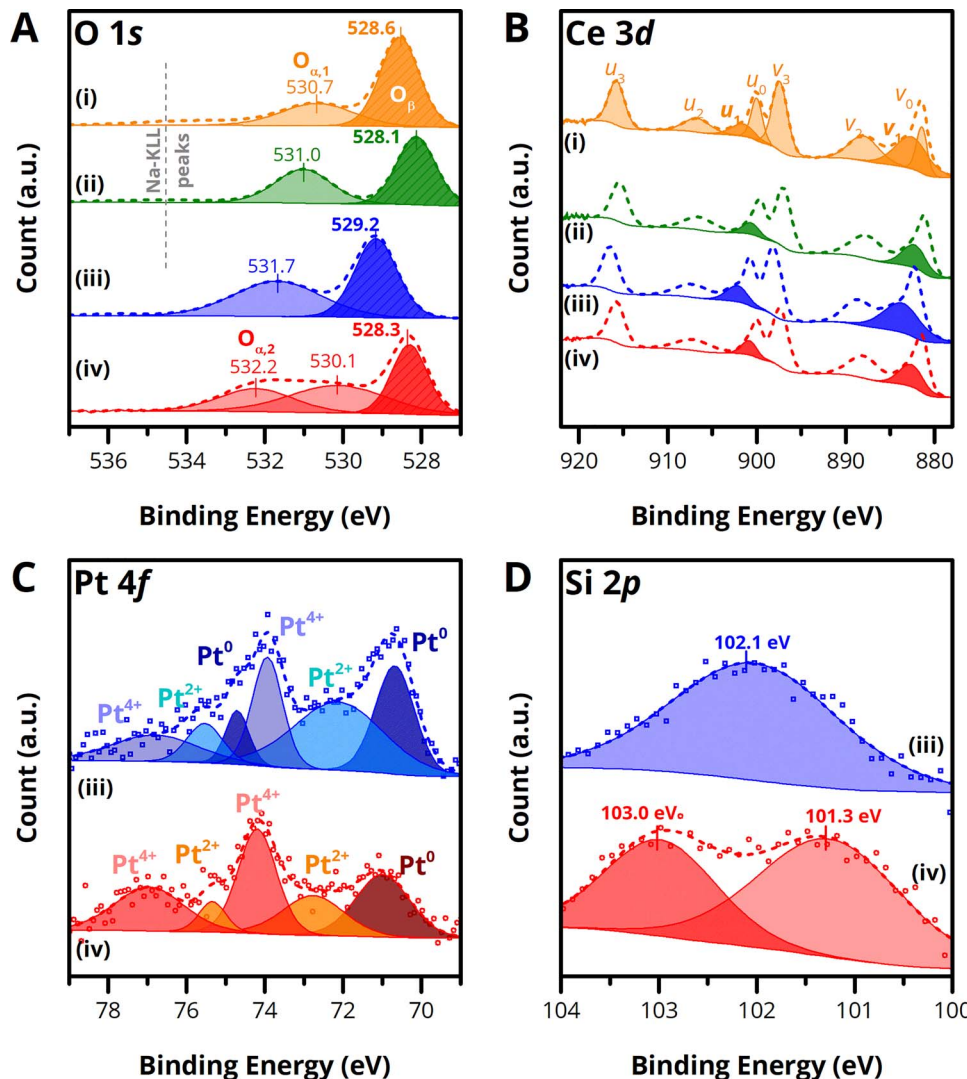
Fig. 6. Deconvoluted XP spectra of aged (i) Ce-NP, (ii) Ce50Pr50-NP, (iii) Pt/Ce-NP and (iv) Pt/Ce50Pr50-NP on (A) O 1s, (B) Ce 3d, (C) Pt 4f and (D) Si 2p core levels.

decrease in surface carbon content. The O_β percentage of the samples seems to increase after the thermal aging, as reported on Table 2, albeit slightly. The aged Pt/Ce-NP sample has more or less a similar trend to the bare supports, in which the O_β/O_α ratio increases, even significantly. The sintering of Pt may contribute to the high percentage of the lattice-like oxygen species on the surface. Interestingly, the aged Pt/Ce50Pr50-NP sample demonstrates three oxygen species, one lattice-like oxygen species O_β at 528.3 eV, one $O_{\alpha,1}$ at 530.1 eV and one additional $O_{\alpha,2}$ at 532.2 eV. Since the segregation of praseodymia on the surface is hardly observed through the XP spectrum of aged Ce50Pr50-NP (only a minor increase in O_β percentage), we speculate that the diversity in oxygen species on the surface of aged Pt/Ce50Pr50-NP may be connected to segregation of platinum nanoparticles and/or silica.

Fig. 5B shows the Ce 3d spectra of the fresh samples. Two peaks at BE ca. 883 eV and 902 eV, denoted herein as v_1 and u_1 respectively, are ascribed to Ce^{3+} cations while the rest of the deconvoluted peaks are ascribed to Ce^{4+} cations [25–27]. The relative abundances of Ce^{3+} cations are also summarized on Table 2. It seems that the quantity of Ce^{3+} cations are higher in Ce − Pr systems. After Pt deposition onto the support, the quantity of Ce^{3+} hardly changed and this is most likely due to the low metal loading. Fig. 6B shows the deconvoluted Ce 3d spectra of the aged samples, where two dark-shaded deconvoluted peaks locate the presence of Ce^{3+} species on the surface. The larger peak area is observed for Ce-NP and Pt/Ce-NP, especially the u_1 peak at around 883 eV. Table 2 also summarizes the relative abundances of Ce^{3+} cations of the aged samples. Compared to the ones of the fresh samples, the abundances of Ce^{3+} are higher in the aged Ce-NP and Pt/Ce-NP samples, yet they are lower in the aged Ce50Pr50-NP and Pt/Ce50Pr50-NP samples. In the case of fresh samples, the presence of praseodymia evidently increases the cerium redox sites on the surface. However, thermally aging the ceria-praseodymia sample, under an oxidizing atmosphere, may lead to the segregation of ceria and praseodymia phases, during which the oxidized Ce^{4+} cations may resurface.

Fig. 5C shows the deconvoluted Pt 4f spectra of the fresh Pt-containing catalysts. According to the literature [28,29], the spectrum can be deconvoluted into three pairs of peaks: (1) the first pair appears at 70.9 eV and 74.8 eV refers to Pt^{00}, (2) the second pair appears at 72.3 eV and 75.6 eV refers to Pt^{2+} and (3) the third pair appears at 74.0 eV and 77.5 eV refers to Pt^{4+}. The first spectrum (blue) belongs to Pt/Ce-NP and demonstrates that the deposited Pt is mainly composed of Pt^{2+} (the quantity is ca. 47%, see Table 2). The zerovalent Pt species also exists in the sample and the quantity nearly equals the Pt^{4+} ones. The second spectrum, on the other hand, belongs to Pt/Ce50Pr50-NP and strikingly shows that the deposited Pt contains around 68%-atom of Pt^{4+}. Pt^{00} species exists rather insignificantly in the sample. Fig. 6C shows the deconvoluted Pt 4f spectra of the aged Pt/Ce-NP and Pt/Ce50Pr50-NP. The spectra of the two samples evidently show the high intensity Pt^{00} peak at 70.9–71 eV and Pt^{4+} peak at 73.9–74.1 eV. The relative abundances of Pt species of the aged samples are also reported in Table 2. Slight increases in Pt^{00} and Pt^{4+} abundances are observed for aged Pt/Ce-NP. The higher-oxidation state Pt species, like Pt^{4+} and Pt^{2+}, are presumably transformed to Pt^{00} during the thermal aging due to the sintering of nanoparticles, while the relatively constant abundance of Pt^{4+} in the sample despite the aging might be due to the strong Pt – ceria interaction [30]. A much higher increase in Pt^{00} species is observed for aged Pt/Ce50Pr50-NP, yet it is also compensated by a more significant loss of Pt^{4+} species. This suggests that the bonds between Pt nanoparticles and ceria-praseodymia support are easily enfeebled by the thermal aging and therefore the segregation of Pt particles becomes inevitable.

Fig. 6D shows the Si 2p spectra of the Pt-containing catalysts. The spectra give insight into Pt nanoparticles stability against sintering under a heat treatment, e.g. calcination. Therefore, we include the analysis of the spectra in the discussion. In general, the spectra of Pt/Ce-NP and Pt/Ce50Pr50-NP exhibit wide peaks centered at about 101.7 eV and 101.2 eV, respectively. We ascribe these peaks to siloxane

(−Si−O−Si−), referring to the literature [31,32]. We have previously suggested that air calcination transforms Si atoms into a siliceous patch that is constituted of repeated siloxanes and able to protect a Pt nanoparticle from enlargement/sintering [12]. Fig. 6D shows the Si 2p spectra of the aged Pt-containing catalysts. The spectrum peak of aged Pt/Ce-NP is slightly shifted to higher BE compared to the one of fresh Pt/Ce-NP (from 101.7 eV to 102.1 eV). This implies that, while most siloxane patches may still exist in the aged sample, some may already undergo transformation to higher oxidation state Si species, possibly silica (SiO_2). More diverse Si species are instead observed for Pt/Ce50Pr50-NP. The first peak at 101.3 eV may be ascribed to siloxane, while the second peak at 103.0 eV may be ascribed to SiO_2. This reinforces the phenomenon of Pt segregation on the surface of Ce50Pr50-NP, which is favored by the thermal aging. The slower Si phase transition observed for Pt/Ce-NP evidences the stronger metal-support interaction between Pt and pure ceria.

Fig. S9 (Supporting Information) finally shows the Pr 3d XP spectra of the fresh ceria-praseodymia catalysts. In general, the two catalysts exhibit two main peaks (m and m') at 932.8 and 952.8 eV, respectively, and their accompanying/satellite peaks (s and s') at 928.2 and 948.6 eV, respectively. The t' peak also appears in the spectra of the two samples at about 957.1 eV and simply refers to extra structure that exists only in $3d_{3/2}$ region [33]. The peak characteristics of the two samples are somewhat similar to those of Pr_2O_3 (Pr^{3+}) yet according to the literature the primary peaks (m, m', s, s' and t') are also indicative of PrO_2 (Pr^{4+}) [34,35]. In addition, the peak f' at about 965 eV strongly suggests the presence of Pr^{4+} as it only appears in PrO_2 [36]. Therefore, the proportion of Pr^{3+} and Pr^{4+} cannot simply be quantified via peak deconvolution. It can only be inferred that both Pr^{3+} and Pr^{4+} coexist in the sample.

3.3. Catalyst reducibility

We have chosen CO-TPR technique to characterize the reducibility of our catalysts because CO, reducing by nature, is found abundantly in Diesel exhaust. During the reduction, we expect that CO consume different oxygen species, originating from both surface and crystal bulk of the catalysts. Since the release of one species is highly temperature-dependent, one would expect at the end that the reduction curve be comprised of multiple peaks. Through curve deconvolution, we have equally estimated the quantity of oxygen consumed during the reduction.

Fig. 7 summarizes the result from CO-TPR. Fig. S10 (Supporting Information) shows the deconvoluted reduction curves for all fresh samples. In addition, we also include the reduction curve of Pr-NP, the pure praseodymium oxide sample for comparison. Table 3 contains more details about the total oxygen of the samples consumed during the reduction as well as the amount of oxygen possibly generated via metal-support interaction. Generally, the highest reduction intensity has been demonstrated by the praseodymia-containing catalysts. The reduction of Pr-NP, in particular, results in a high conversion of CO (almost 50%) and reaches its peak at about 530 °C. Similar reduction profile of praseodymium oxide has also been reported elsewhere [37]. The amount of oxygen consumed during the reduction until 600 °C has been estimated at about 0.16 mmol. Ce-NP, on the other hand, has the lowest intensity of reduction in the series, yet it shows better reduction light-off behavior; the temperature at which the CO conversion begins seems lower than that of Pr-NP.

The reduction profile of the mixed oxide sample, Ce50Pr50-NP, simply reflects a hybrid of Ce-NP and Pr-NP behaviors: lower light-off and reduction peak temperature but sufficiently high reduction intensity. The reason behind the optimum reducibility of this material lies in the fact that praseodymia increases not only the surface oxygen population but also surface cerium redox sites, as evidenced earlier by XPS data (vide supra). The amount of oxygen consumed during the reduction of Ce50Pr50-NP is around 0.11 mmol. We suggest that mixing
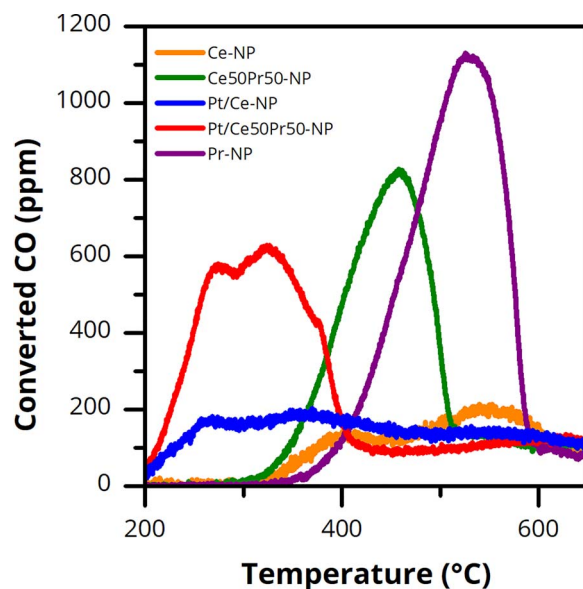
Fig. 7. Evolution of CO_2 during CO-TPR represented by converted CO concentration (ppm) as a function of temperature.

Table 3
Estimated quantity of oxygen species (mmol) derived from CO-TPR curve deconvolution.

Sample	Type of oxygen		O_{Pt}/Pt^c ratio
	$O_{TOT}{}^a$	$O_{Pt}{}^b$	
Pr-NP	0.162	–	–
Ce-NP	0.054	–	–
Ce50Pr50-NP	0.109	–	–
Pt/Ce-NP	0.092	0.009	4.67
Pt/Ce50Pr50-NP	0.115	0.046	33.1

[a] all oxygen species consumed during the low-temperature reduction ($\ll 600\,°C$).
[b] oxygen species due to strong metal-support interaction (SMSI) between platinum and ceria/ceria-praseodymia.
[c] mmol of Pt calculated using the estimated Pt content from ICP-AES.

equimolarly ceria with praseodymia results in a weakening of Ce−O bond, leading to more reduced cerium sites and eventually to more available oxygen species for a reaction on the surface. This has also been suggested by the results from XPS, in which the abundance of lattice oxygen species becomes lower in the case of Ce50Pr50-NP

The reduction of Pt-containing samples (blue and red curves representing Pt/Ce-NP and Pt/Ce50Pr50-NP, respectively) results in an early emergence of CO_2 at about 250 °C. The oxygen species involved in this temperature range can be denoted as "O_{Pt}", since this is undoubtedly due to the strong metal-support interaction (the so called "SMSI") between Pt and ceria. In the classical H_2 reduction, the presence of Pt on ceria helps improve hydrogen transfer from bulk to ceria surface via dissociative adsorption and spillover [38,39]. However, in the case of CO reduction, CO does not dissociate on the surface of Pt. Two mechanisms have been proposed by Serre et al: (1) C−O bond weakening near Pt−CeO2 interface and (2) Ce−O bond weakening near Pt sites [40]. In the first mechanism, CO is firstly adsorbed to Pt, then undergoes C−O bond weakening due to electron donation from carbon (lone pair on 5σ orbital) to d orbitals of Pt and electron back-donation from d orbitals of the metal to 2π*-antibonding of carbon. CO molecule adsorbed near Pt−CeO2 interface will easily access oxygen atom from ceria and upon reaction will quickly desorb as CO_2. In the second mechanism, Pt is believed to modify redox properties of ceria, weakening cerium − oxygen bond strength near Pt−CeO2 interface. However, our finding with XPS (vide supra) have shown that after impregnation with Pt-NPs the estimated quantity of Ce^{3+} in the sample hardly changes.
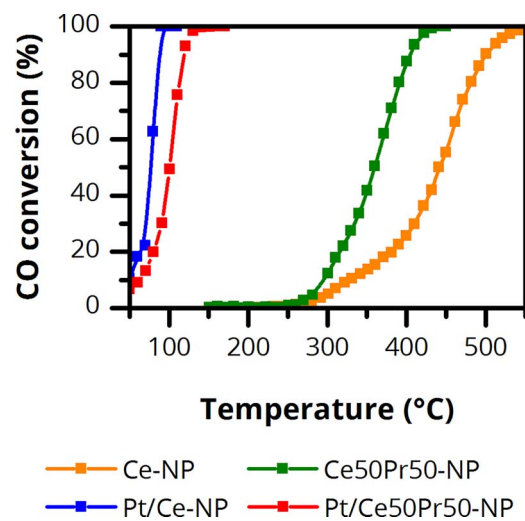

Fig. 8. CO conversion to CO_2 as a function of temperature during CO oxidation test.

We surmise that the second mechanism is not likely to occur at low metal loading. It is worth noticing that the quantity of O_{Pt}, as reported in Table 3, seems to depend on the support. The quantity appears higher for Pt/Ce50Pr50-NP than that for Pt/Ce-NP. Additionally, the O_{Pt}-to-Pt ratio for Pt/Ce50Pr50-NP is much greater than that for Pt/Ce-NP. The reason behind this phenomenon remains unclear and scarcely studied in the literature, yet we believe there is a unique interaction between Pt and ceria-praseodymia during the reduction whose mechanism does not conventionally conform to the interfacial reduction of Pt – ceria.

3.4. Catalytic activity test

3.4.1. CO oxidation

Fig. 8 shows the CO conversion into CO_2 over the prepared catalysts as a function of temperature. Ce-NP appears to be the least performing catalyst in the series, while the presence of praseodymia in Ce50Pr50-NP seems to improve the catalytic activity. This can be linked to the fact that the presence of praseodymia betters the redox properties of ceria, as previously highlighted in the discussion of XPS and TPR data. The activity of Pt-containing catalysts, as one would expect, is much higher than that of Pt-free catalysts. The difference in $T_{50\%}$, the temperature at which 50% conversion of CO is achieved, is around 250 °C in the case of Pt/Ce-NP and around 400 °C in the case of Pt/Ce50Pr50-NP. As seen on Fig. 8, the conversion of CO mediated by Pt nanoparticles occurs already at 50 °C, albeit little (ca. 10% and 6% for Pt/Ce-NP and Pt/Ce50Pr50-NP, respectively) and finishes at around 100 °C. The trend of Pt-containing catalyst is somewhat different from that of Pt-free catalyst: the apparent activity is higher in Pt/Ce-NP. This could be due to the better interaction between Pt and Ce than that between Pt and Ce−Pr system. This comes as no surprise as the early evidences from electron microscopy and XPS data of fresh and aged samples have all converged to demonstrating the scarce interaction between Pt and ceria-praseodymia.

3.4.2. NO oxidation

Fig. 9 shows the results from NO oxidation catalytic activity tests with the prepared catalysts. Fig. 9A shows the profile of NO_2 percentage in the NO_x mixture as a function of temperature during the tests with ramping mode. Ce-NP (orange curve) has evidently the lowest catalytic activity towards NO oxidation in the series. The reaction over this material lights off at ca. 350 °C and reaches its maximum conversion (ca. 20% of NO inlet) at 500 °C. The impregnation of Ce-NP with Pt nanoparticles without a doubt enhances the activity of Ce-NP towards the reaction. The reaction lights off very early even at 200 °C and
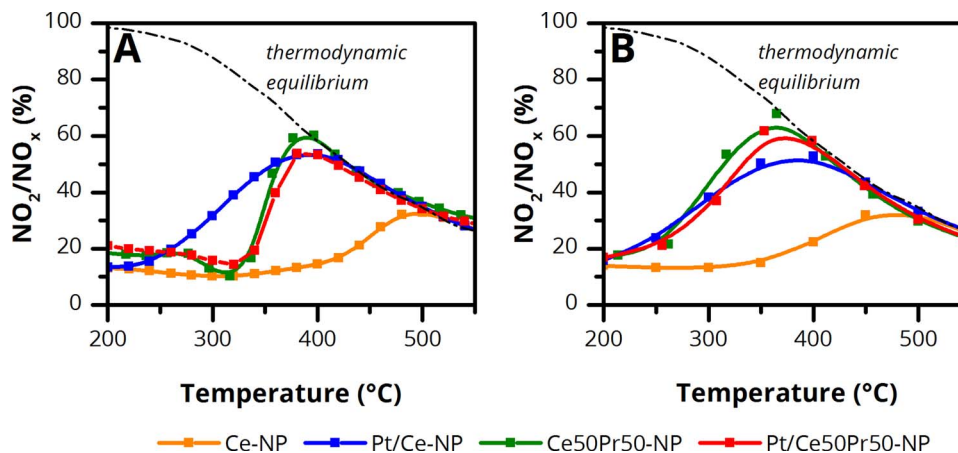
Fig. 9. NO_2 percentage in NO_x as a function of temperature during NO oxidation test with (A) ramping and (B) isothermal heating modes.

reaches its maximum conversion (ca. 55% of NO inlet, much higher than that of pure Ce-NP) at much lower temperature, 400 °C. Much to our surprise, Ce50Pr50-NP (green curve) demonstrates an unusual profile as the concentration of NO_2 appears to decrease between 250 and 350 °C. Similar trend is also observed in the case of Pt/Ce50Pr50-NP. We surmise that, in the observed temperature interval, our ceria-praseodymia catalyst adsorbs NO_2. Above 350 °C, the NO_2 percentage rises steeply, even surpassing the peak of Pt/Ce-NP. We have performed separate calculation of NO conversion for Ce50Pr50-NP and we discovered that maximum conversion attainable by the catalyst is ca. 78%, the value of which exceeds the one of Pt/Ce-NP. The addition of Pt onto Ce50Pr50-NP surface does not seem to give much impact on the catalytic activity as the profile of Pt/Ce50Pr50-NP (red curve) is somewhat similar to that of Ce50Pr50-NP.

Due to the NO_2 adsorption phenomenon on the surface of Ce50Pr50-NP, we have retested the catalysts under isothermal conditions. As it has been explained in the previous section, we performed the test by heating the reactor stepwise by 50 °C from the initial reactor temperature (50 °C); in each step, the temperature was kept constant for an isothermal treatment till the stabilization of gas concentrations. Fig. 9B shows the results of this test in terms of NO_2 percentage in NO_x mixture. All the catalysts in the second test exhibit normal bell curves. Ceria-praseodymia samples no longer demonstrate the decreasing trend at low temperatures, indicating the success of this test in avoiding any adsorption phenomena and in revealing the true nature of the reaction. As expected, ceria-praseodymia catalysts, undecorated or decorated by Pt-NPs, appear to be much more active than Pt/Ce-NP. The rate of NO_2 production at low temperature is evidently higher for ceria-praseodymia catalysts compared to that for Pt/Ce-NP. In this test, we can also observe that the activity of Pt/Ce50Pr50-NP is similar to that of Ce50Pr50-NP. We speculate that the effect of praseodymia is so prevalent towards NO oxidation that Pt mediation does not seem to function.

3.4.3. Soot oxidations

Fig. 10 summarizes soot conversion, CO and CO_2 concentrations as functions of temperature during the tests with soot oxidation. Figures on the first column (Fig. 10A – C – E) refer to the results obtained in normal, NO_x-free soot oxidation while the others on the second column (Fig. 10B – D – F) refer to the results obtained in NO_x-assisted soot oxidation. Table 4 also summarizes the $T_{10\%}$, $T_{50\%}$ and $T_{90\%}$ data of the prepared catalysts. In the absence of NO_x, the catalytic activity of Ce-NP catalysts is evidently lower than that of Ce50Pr50 catalysts regardless of platinum content. This is in a good agreement with our previous work that has concluded the positive effect of praseodymium in ceria towards the catalytic activity of NO_x-free soot oxidation [9]. Irrespective of support, the effect of Pt is rather negligible on the reaction as the specific reaction rates hardly change in the case of Pt-impregnated

catalysts.

Fig. 10C and E exhibit the CO_2 and CO concentration evolution during the tests with NO_x-free soot oxidation. The reaction over Pt/Ce-NP and Pt/Ce50Pr50-NP seems to yield higher CO_2 concentration than that over Ce-NP and Ce50Pr50-NP. Conversely, CO concentrations evolving from the reaction over Pt/Ce-NP and Pt/Ce50Pr50-NP are much lower than those coming from the reaction over Ce-NP and Ce50Pr50-NP. This highlights the role of Pt as the excellent catalyst for CO oxidation, as discussed earlier. Although it only indirectly benefits the whole catalytic activity, the present of Pt is somewhat necessary to increase CO_2 selectivity.

Fig. 10B shows the soot conversion as a function of temperature over the prepared catalysts during the test with NO_x-assisted soot oxidation. Ce-NP (orange curve) has certainly the lowest activity in the series due to the absence of Pt. While it is obvious that Pt/Ce-NP (blue curve) shifts the reaction temperature to lower range, Ce50Pr50-NP (green curve) evidently outperforms Pt/Ce-NP. The excellent performance of Ce—Pr system likely roots in the active interaction between Pr sites and NO_2. From the results obtained in the tests with NO oxidation, we fathom that the presence of praseodymia in ceria matrix not only boosts the conversion of NO to NO_2 but also facilitates NO_2 adsorption on the surface. Meanwhile, the presence of platinum nanoparticles on ceria only gives NO to NO_2 conversion yet it does not promote NO_2 adsorption. We surmise insofar that the success of NO_x-assisted soot oxidation is also determined, rather crucially, by the adsorption of NO_2 on the surface of ceria. The adsorbed NO_x species, since they are fixated on the surface, can be in direct contact with soot in soot-catalyst interface, thus initiating the oxidation process. Interestingly, Pt/Ce50Pr50-NP seems to perform similarly to Ce50Pr50-NP. The $T_{50\%}$ of this catalyst (456 °C) is only lower by ca. 7° compared to that of Ce50Pr50-NP (463 °C). This finding signifies that the presence of Pt sites on the surface of ceria-praseodymia seems rather unnecessary. The Ce—Pr system is so powerfully reactive towards NO_x species that the effect of Pt is almost negligible. The sole Ce50Pr50-NP catalyst is certainly appealing from the economic viewpoint since the use of Pt can be eliminated. However, it is also important to know the selectivity of the catalyst to CO_2. Fig. 10D and F show CO_2 and CO concentrations as a function of temperature obtained during the test with NO_x-assisted soot oxidation. Expectedly, the selectivity to CO_2 is the highest in the case of Pt-containing catalysts, while bare ceria-based supports still produce a considerable amount of CO. Similar to the finding in the tests with NO_x-free soot oxidation, the most striking function of Pt in Pt/Ce50Pr50-NP is to maintain the CO_2 selectivity of the reaction.

Fig. 11 shows the transient profile of CO_2 concentration (%) during the isothermal oxidation of soot, in the presence of NO_x, at 400 °C. Upon the introduction of oxidants, CO_2 emanates quickly in the case of ceria-praseodymia catalysts. The peak of CO_2 concentration at the beginning of the reaction is the highest for Pt/Ce50Pr50-NP (CO_2
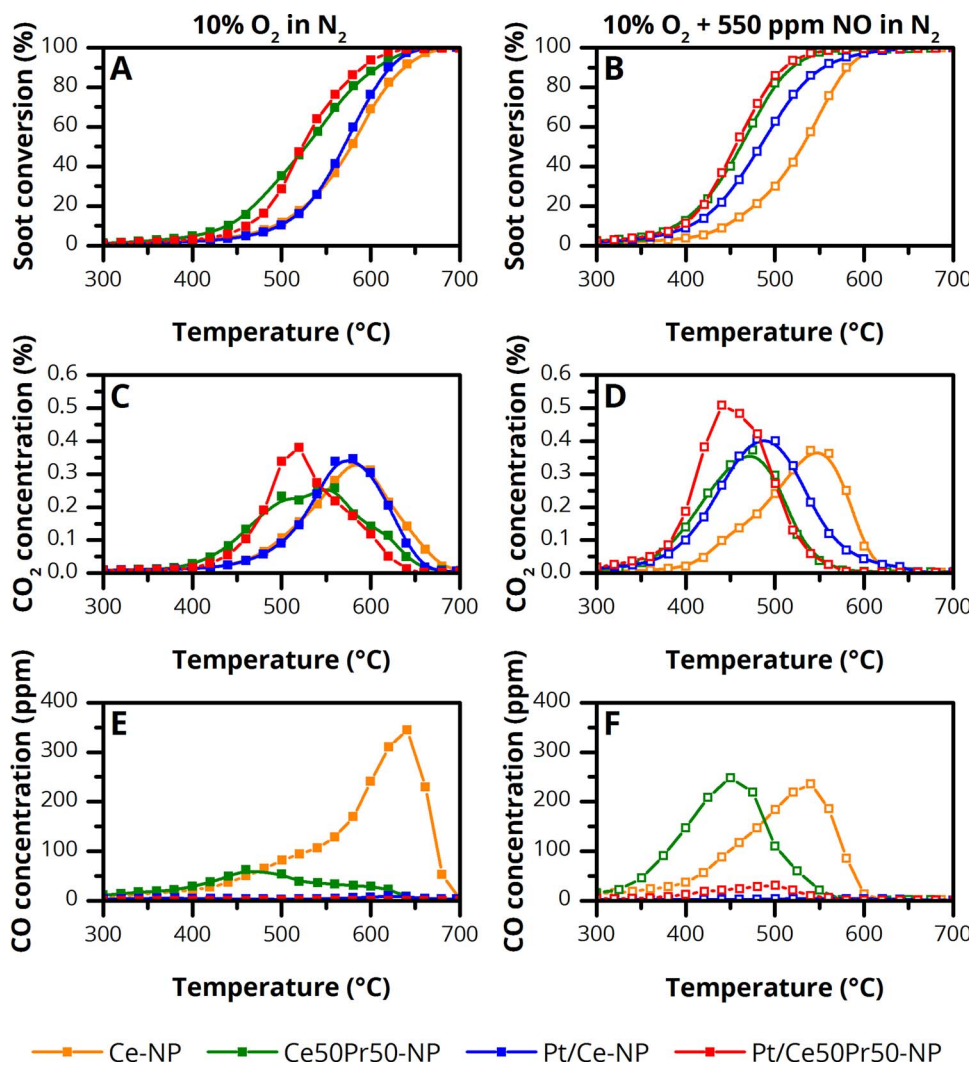
Fig. 10. Soot conversion, CO_2 and CO concentrations as a function of temperature during the test with (A – C – E) NO_x-free soot oxidation and (B – D – F) NO_x-assisted soot oxidation.

Table 4
Results from soot oxidation catalytic tests with the fresh samples in the absence and the presence of NO_x.

In the absence of NO_x (10% O_2 in N_2)

Sample	$T_{10\%}$ (°C)	$T_{50\%}$ (°C)	$T_{90\%}$ (°C)
Ce-NP	494	579	637
Ce50Pr50-NP	441	527	609
Pt/Ce-NP	499	570	620
Pt/Ce50Pr50-NP	463	523	590

In the presence of NO_x (550 ppm NO + 10% O_2 in N_2)

Sample	$T_{10\%}$ (°C)	$T_{50\%}$ (°C)	$T_{90\%}$ (°C)
Ce-NP	446	531	580
Ce50Pr50-NP	391	463	516
Pt/Ce-NP	406	484	552
Pt/Ce50Pr50-NP	396	456	509

Fig. 11. Transient profile of CO_2 concentration (%) during the test with isothermal NO_x-assisted soot oxidation (T = 400 °C).

concentration at peak point ca. 0.32%), while that for Ce50Pr50-NP ranks the second (CO_2 concentration at peak point ca. 0.21%). Despite the similarity in catalytic activity in the previous tests, the performances of the two catalysts appear distinguishable in this test. However, we suggest that higher CO_2 signal in the case of Pt/Ce50Pr50-NP is due to better oxygen transfer from bulk to catalyst − soot interface governed by Pt-NPs (via "spillover" mechanism). After 100 min, the

reaction mediated by these two catalysts seems to terminate. As observed, the activity of Pt/Ce-NP is much lower than Ce50Pr50-NP. The CO_2 peak is noticed rather scarcely at the beginning of the reaction (concentration at ca. 0.13%). The oxidation of soot occurs much slower
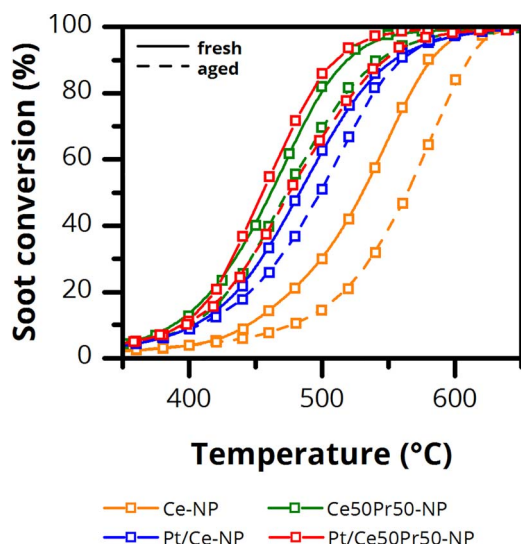
Fig. 12. Comparison of catalytic activity, in terms of soot conversion, between fresh (straight lines) and aged catalysts (dashed lines).

than ceria-praseodymia catalysts and the CO_2 concentration remains higher after 100 min of reaction. Ce-NP finally has the lowest activity towards the isothermal oxidation. The CO_2 peak concentration is noticeable at ca 0.06%. The reaction occurs very slowly and remains incomplete after 100 min.

3.4.4. Catalyst stability

Stability test has been carried out to see how distant the catalytic activity of the aged materials with respect to the fresh ones. As stated previously in Experimental section, we used NO_x-assisted soot oxidation as our probe reaction. Fig. 12 exhibits the soot conversion as a function of temperature over the prepared catalysts. Straight curves represent the conversion over fresh catalysts while dashed curves represent the conversion over aged catalysts. Fig. 13 summarizes the $T_{50\%}$ for each catalyst, fresh and aged. As seen on Fig. 12, the activity of Ce-NP evidently declines when aged with the $T_{50\%}$ offset at about 6% (extracted from Fig. 13). Such a decrease in catalytic activity has been predicted from previous characterization data, which have demonstrated the loss of surface area and reactive facets due to post-aging surface truncation. The activity of aged Ce50Pr50-NP only slightly decreases from that of the fresh one and the $T_{50\%}$ offset is the lowest among the catalysts (ca. 2%). This finding somewhat disagrees the prior spectroscopic evidences from XRD and XPS, which have demonstrated the possibility of

segregation of praseodymia post-thermal aging. However, one should point out the fact that the reaction also involves NO_2 as one of the oxidants and the material is very NO_2-adsorptive even when it is thermally aged (the NO oxidation profile of the aged samples is not reported herein for the sake of brevity). Therefore, in the case of aged ceria-praseodymia, NO_2 adsorption becomes a determinant of the catalytic activity of aged Ce50Pr50-NP towards NO_x-assisted soot oxidation.

Pt/Ce-NP and Pt/Ce50Pr50-NP have medium $T_{50\%}$ offsets at about 3% and 4%, respectively. Compared to aged Ce-NP, aged Pt/Ce-NP evidently has a lower soot conversion temperature. This means that, even after the thermal aging, the impregnated Pt nanoparticles still functioned. The particle sintering is indeed inevitable as it has been revealed earlier via electron microscopy by the enlargement of Pt nanoparticles (average sintered size of 10 nm). Nevertheless, the analysis with deconvoluted Si 2*p* XP spectra has demonstrated that the siloxane may remain in the structure as the small Si peak shift to the higher binding energy is tolerable. In addition, the Pt^{4+} species, which is indicative of SMSI, is also present in a comparable abundance on the surface of both fresh and aged sample. The activity of aged Pt/Ce50Pr50-NP, in contrast, appears to be similar to that of aged Ce50Pr50-NP. The deconvoluted Pt 4*f* XP spectrum of aged Pt/Ce50Pr50-NP has demonstrated a severe loss of Pt^{4+} species after the thermal aging. Moreover, the Si 2*p* spectrum of the sample has also evidenced the presence of two Si phases (silica and siloxane), which might indicate the segregation of silica from the Pt − Si system. This hypothesis is further strengthened by the increase in Si content observed on the surface of aged Pt/Ce50Pr50-NP, as evidenced by the wide-scan XP spectrum. These spectroscopic evidences also indirectly suggest that the accompanying silicon atoms not only interact with the platinum particles but also with the support. Finally, we suggest that the strength of metal-support interaction in this case is dependent on the support itself. Such an interaction seems to be more easily maintained on the surface of ceria rather than on the surface of ceria-praseodymia

4. Conclusion

The series of tests in this work has finally concluded the proven performance of nanostructured equimolar ceria-praseodymia (Ce50Pr50-NP) towards NO_x-assisted soot oxidation. The intrinsic activity of this material is even much higher than its Pt/ceria counterpart. We reason that such a high activity most likely originates from the strong interaction between ceria-praseodymia and NO_2 via adsorption. The addition of Pt nanoparticles on the surface of Ce50Pr50-NP appears unnecessary as the effect of Pr on the catalytic activity prevails. The tests with aged samples have led us to various suggestions, such as:

a the NO_x-assisted soot oxidation catalytic activity over the aged ceria-praseodymia remains relatively high in the series due to its beneficial NO_x-adsorptive properties

b Pt particle sintering is inevitable on the surface of ceria-praseodymia, likely due to weaker metal-support interaction

Appendix A. Supplementary data

Supplementary data associated with this article can be found, in the online version, at https://doi.org/10.1016/j.apcatb.2017.12.048.
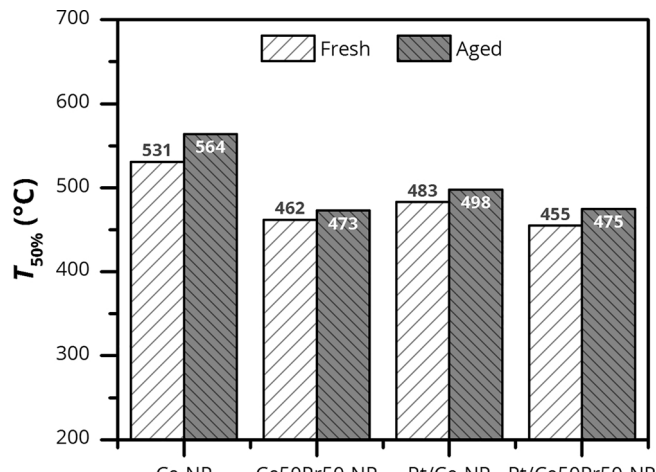
Fig. 13. Results of stability tests in terms of $T_{50\%}$ of fresh (white bar) and aged catalysts (gray bar).

References

[1] A. Trovarelli, Catalytic properties of ceria and CeO2 – containing materials, Catal. Rev. 38 (1996) 439–520.
[2] E. Aneggi, M. Boaro, C. de Leitenburg, G. Dolcetti, A. Trovarelli, Insights into the redox properties of ceria-based oxides and their implications in catalysis, J. Alloys Compd. 408 (2006) 1096–1102.
[3] E. Aneggi, M. Boaro, S. Colussi, C. de Leitenburg, A. Trovarelli, Ceria-Based Materials in Catalysis, (2016), pp. 209–242.
[4] H.C. Yao, Y.F. Yu Yao, Ceria in automotive exhaust catalysts I. Oxygen storage, J. Catal. 86 (1984) 254–265.
[5] E. Mamontov, T. Egami, R. Brezny, M. Koranne, S. Tyagi, Lattice defects and oxygen storage capacity of nanocrystalline ceria and ceria-Zirconia, J. Phys. Chem. B 104 (47) (2000) 11110–11116.
[6] M. Piumetti, S. Bensaid, N. Russo, D. Fino, Nanostructured ceria-based catalysts for soot combustion: investigations on the surface sensitivity, Appl. Catal. B Environ. 165 (2015) 742–751.
[7] E. Aneggi, D. Wiater, C. de Leitenburg, J. Llorca, A. Trovarelli, Shape-Dependent activity of ceria in soot combustion, ACS Catal. 4 (2014) 172–181.
[8] S. Liu, X. Wu, J. Tang, P. Cui, X. Jiang, C. Chang, W. Liu, Y. Gao, M. Li, D. Weng, An exploration of soot oxidation over CeO2-ZrO2 nanocubes: do more surface oxygen vacancies benefit the reaction? Catal. Today 281 (2017) 454–459.
[9] T. Andana, M. Piumetti, S. Bensaid, N. Russo, D. Fino, R. Pirone, Nanostructured ceria-praseodymia catalysts for diesel soot combustion, Appl. Catal. B Environ. 197 (2016) 125–137.
[10] M. Piumetti, S. Bensaid, N. Russo, D. Fino, Investigations into nanostructured ceria–zirconia catalysts for soot combustion, Appl. Catal. B Environ. 180 (2016) 271–282.
[11] M. Piumetti, T. Andana, S. Bensaid, D. Fino, N. Russo, R. Pirone, Ceria-based nanomaterials as catalysts for CO oxidation and soot combustion: effect of Zr-Pr doping and structural properties on the catalytic activity, AIChE J. 63 (2017) 216–225.
[12] T. Andana, M. Piumetti, S. Bensaid, L. Veyre, C. Thieuleux, N. Russo, D. Fino, E.A. Quadrelli, R. Pirone, Ceria-supported small Pt and Pt3Sn nanoparticles for NOx-assisted soot oxidation, Appl. Catal. B Environ. 209 (2017) 295–310.
[13] T. Andana, M. Piumetti, S. Bensaid, L. Veyre, C. Thieuleux, N. Russo, D. Fino, E.A. Quadrelli, R. Pirone, CuO nanoparticles supported by ceria for NOx-assisted soot oxidation: insight into catalytic activity and sintering, Appl. Catal. B Environ. 216 (2017) 41–58.
[14] K. Krishna, A. Bueno-López, M. Makkee, J.A. Moulijn, Potential rare-earth modified CeO2 catalysts for soot oxidation: part III. Effect of dopant loading and calcination temperature on catalytic activity with O2 and NO + O2, Appl. Catal. B Environ. 75 (2007) 210–220.
[15] N. Guillén-Hurtado, A. García-García, A. Bueno-López, Active oxygen by Ce?Pr mixed oxide nanoparticles outperform diesel soot combustion Pt catalysts, Appl. Catal. B Environ. 174 (2015) 60–66.
[16] K. Moseley, P.M. Maitlis, Bis- and tris-(dibenzylideneacetone)platinum and the stabilization of zerovalent complexes by an unsaturated ketone, J. Chem. Soc. D Chem. Commun. 982 (1971).
[17] K. Pelzer, M. Hävecker, M. Boualleg, J.-P. Candy, J.-M. Basset, Stabilization of 200-Atom platinum nanoparticles by organosilane fragments, Angew. Chemie 123 (2011) 5276–5279.
[18] H.-X. Mai, L.-D. Sun, Y.-W. Zhang, R. Si, W. Feng, H.-P. Zhang, H.-C.L. Liu, C.-H. Yan, Shape-Selective synthesis and oxygen storage behavior of ceria nanopolyhedra, Nanorods Nanocubes (2005).
[19] K. Zhou, Y. Li, Catalysis based on nanocrystals with well-Defined facets, Angew. Chemie Int. Ed. 51 (2012) 602–613.
[20] T. Andana, M. Piumetti, S. Bensaid, L. Veyre, C. Thieuleux, N. Russo, D. Fino, E.A. Quadrelli, R. Pirone, Ceria-supported small Pt and Pt3Sn nanoparticles for NOx-assisted soot oxidation, Appl. Catal. B Environ. 209 (July 15) (2017) 295–310.
[21] L. Soler, A. Casanovas, C. Escudero, V. Pérez-Dieste, E. Aneggi, A. Trovarelli, J. Llorca, Ambient pressure photoemission spectroscopy reveals the mechanism of carbon soot oxidation in ceria-Based catalysts, ChemCatChem 8 (2016) 2748–2751.
[22] Y. Zhang, J. Deng, H. Zhang, Y. Liu, H. Dai, Three-dimensionally ordered macroporous Pr6O11 and Tb4O7 with mesoporous walls: preparation, characterization, and catalytic activity for CO oxidation, Catal. Today 245 (2015) 28–36.
[23] J.-C. Dupin, D. Gonbeau, P. Vinatier, A. Levasseur, Systematic XPS studies of metal oxides, hydroxides and peroxides, Phys. Chem. Chem. Phys. 2 (2000) 1319–1324.
[24] G. Grzybek, P. Stelmachowski, S. Gudyka, P. Indyka, Z. Sojka, N. Guillén-Hurtado, V. Rico-Pérez, A. Bueno-López, A. Kotarba, Strong dispersion effect of cobalt spinel active phase spread over ceria for catalytic N2O decomposition: the role of the interface periphery, Appl. Catal. B Environ. 180 (2016) 622–629.
[25] M. Romeo, K. Bak, J. El Fallah, F. Le Normand, L. Hilaire, XPS Study of the reduction of cerium dioxide, Surf. Interface Anal. 20 (1993) 508–512.
[26] M. Kurnatowska, W. Mista, P. Mazur, L. Kepinski, Nanocrystalline Ce1-xRuxO2 – Microstructure, stability and activity in CO and soot oxidation, Appl. Catal. B Environ. 148–149 (2014) 123–135.
[27] T. Andana, M. Piumetti, S. Bensaid, N. Russo, D. Fino, R. Pirone, CO and soot oxidation over Ce-Zr-Pr oxide catalysts, Nanoscale Res. Lett. 11 (2016) 278.
[28] F. Grasset, P. Alphonse, C. Labrugère, J. Darriet, A. Rousset, Correlation between the Pt2+/Pt4+ ratio and the catalytic activity for the CO oxidation of Ba12[BaxPt3-x]Pt6O27 (0 ≤ x ≤ 3), Mater. Res. Bull. 34 (1999) 2101–2108.
[29] C. Nethravathi, E.A. Anumol, M. Rajamathi, N. Ravishankar, Highly dispersed ultrafine Pt and PtRu nanoparticles on graphene: formation mechanism and electrocatalytic activity, Nanoscale 3 (2011) 569–571.
[30] Y. Nagai, T. Hirabayashi, K. Dohmae, N. Takagi, T. Minami, H. Shinjoh, S. Matsumoto, Sintering inhibition mechanism of platinum supported on ceria-based oxide and Pt-oxide-support interaction, J. Catal. 242 (2006) 103–109.
[31] K. Jradi, C. Daneault, B. Chabot, Chemical surface modification of glass beads for the treatment of paper machine process waters, Thin Solid Films. 519 (2011) 4239–4245.
[32] No Title, (n.d.). http://www.xpsfitting.com/2012/01/silicon.html.
[33] J. Gurgul, M.T. Rinke, I. Schellenberg, R. Pöttgen, The antimonide oxides REZnSbO and REMnSbO (RE = Ce, Pr) −An XPS study, Solid State Sci. 17 (2013) 122–127.
[34] S. Lütkehoff, M. Neumann, A. Ślebarski, 3 d and 4 d x-ray-photoelectron spectra of Pr under gradual oxidation, Phys. Rev. B 52 (1995) 13808–13811.
[35] H. Ogasawara, A. Kotani, R. Potze, G.A. Sawatzky, B.T. Thole, Praseodymium 3 d − and 4 d −core photoemission spectra of Pr 2 O 3, Phys. Rev. B 44 (1991) 5465–5469.
[36] A. Bianconi, A. Kotani, K. Okada, R. Giorgi, A. Gargano, A. Marcelli, T. Miyahara, Many-body effects in praesodymium core-level spectroscopies of PrO 2, Phys. Rev. B 38 (1988) 3433–3437.
[37] J. Giménez-Mañogil, N. Guillén-Hurtado, S. Fernández-García, X. Chen, J.J. Calvino-Gámez, A. García-García, Ceria-Praseodymia mixed oxides: relationships between redox properties and catalytic activities towards NO oxidation to NO2 and CO-PROX reactions, Top. Catal. 59 (2016) 1065–1070.
[38] P. Ciambelli, V. Palma, A. Ruggiero, Low temperature catalytic steam reforming of ethanol. 1. The effect of the support on the activity and stability of Pt catalysts, Appl. Catal. B Environ. 96 (2010) 18–27.
[39] K.-R. Hwang, J.-S. Park, S.-K. Ihm, Si-modified Pt/CeO2 catalyst for a single-stage water-gas shift reaction, Int. J. Hydrogen Energy 36 (2011) 9685–9693.
[40] C. Serre, F. Garin, G. Belot, G. Maire, Reactivity of Pt/Al2O3 and Pt-CeO2Al2O3 catalysts for the oxidation of carbon monoxide by oxygen I. catalyst characterization by TPR using CO as reducing agent, J. Catal. 141 (1993) 1–8.